Nonlinear Dynamics **11:** 37–59, 1996.

Non-Periodic Motions of a Jeffcott Rotor with Non-Linear Elastic Restoring Forces

G. ADILETTA, A. R. GUIDO, and C. ROSSI
Dipartimento di Ingegneria Meccanica per l'Energetica, Università degli Studi "Federico II", Napoli, Italy

(Received: 29 June 1995; accepted: 28 November 1995)

Abstract. The conditions that give rise to non-periodic motions of a Jeffcott rotor in the presence of non-linear elastic restoring forces are examined. It is well known that non-periodic behaviours that characterise the dynamics of a rotor are fundamentally a consequence of two aspects: the non-linearity of the hydrodynamic forces in the lubricated bearings of the supports and the non-linearity that affects the elastic restoring forces in the shaft of the rotor. In the present research the analysis was restricted to the influence of the non-linearity that characterises the elastic restoring forces in the shaft, adopting a system that was selected the simplest as possible. This system was represented by a Jeffcott rotor with a shaft of mass that was negligible respect to the one of the disk, and supported with ball bearings. In order to check in a straightforward manner the non-linearity of the system and to confirm the results obtained through theoretical analysis, an investigation was carried out using an experimental model consisting of a rotating disk fitted in the middle of a piano wire pulled taut at its ends but leaving the tension adjustable. The adopted length/diameter ratio was high enough to assume the wire itself was perfectly flexible while its mass was negligible compared to that of the disk. Under such hypotheses the motion of the disk centre can be expressed by means of two ordinary, non-linear and coupled differential equations. The conditions that make the above motion non-periodic or chaotic were found through numerical integration of the equations of motion. A number of numerical trials were carried out using a 4th order Runge–Kutta routine with adaptive stepsize control. This procedure made it possible to plot the trajectories of the disk centre and the phase diagrams of the component motions, taken along two orthogonal coordinate axes, with their projections of the Poincaré sections. On the basis of the theoretical results obtained, the conditions that give rise to non-periodic motions of the experimental rotor were identified.

Key words: Jeffcott rotor, non-periodic motions.

1. Introduction

It is well known that non-periodic behaviour that affects the dynamics of a rotor is mainly determined both by the non-linear hydrodynamic forces in the lubricated bearings of the supports and the non-linear elastic restoring forces in the shaft of the rotor itself. Another complex behaviour that is worth mentioning is due to the presence of clearances in the support-system of the rotor.

A review of the studies regarding non-linear effects in rotor dynamics is given in [31]. A number of the papers that have been mentioned there deal with simple systems like Jeffcott rotors. Subharmonic and superharmonic responses in a simple rotor, in presence of strong non-linearity that is due to radial clearances and rub in the bearings, are studied in [8, 15]. In similar hypotheses regarding bearings, chaotic responses have been obtained both experimentally and theoretically, and are reported in [23]; bifurcation phenomena with reference to a modified Jeffcott rotor is theoretically investigated in [26]. Non-linear spring characteristics relating to the inclination of the shaft in presence of small clearance in ball bearings are examined in [3, 18, 27]. Stability of circular whirling and chaotic responses in a Jeffcott rotor are investigated in [30]. Internal damping in continuous rotor system with non-linear responses is studied in [2,

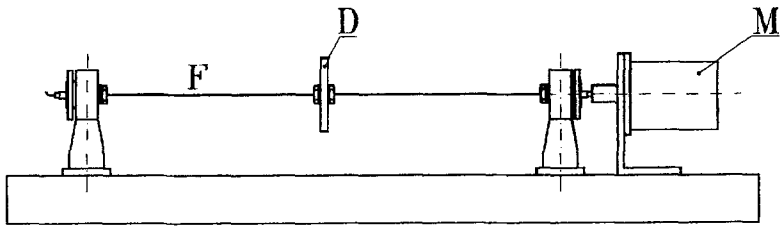

Figure 1. Draft of the Jeffcott rotor.

19, 25, 29]. A theoretical analysis of the chaotic behaviour, due to the non-linear hydrodynamic forces in the lubricated bearings that support an unbalanced rigid rotor, is reported in [28]; a related example of theoretical and experimental results is given in [32].

The present analysis was restricted to the influence of the non-linearity that characterises the elastic restoring forces in the shaft. With this aim a suitable model of rotor was selected, the simplest as possible, represented by a Jeffcott rotor with a shaft of mass that was negligible respect to the one of the disk and rigidly supported with ball bearings. In order to check in a straightforward manner the non-linearity of the system and to confirm the results obtained through theoretical analysis, an investigation was carried out using an experimental model consisting of a rotating disk **D** (Figure 1) fitted in the middle of a piano wire **F**, pulled taut at its ends but leaving the tension adjustable. The adopted length/diameter ratio was high enough to assume the wire itself as perfectly flexible while its mass was negligible compared to that of the disk.

The system is symmetrical (with respect to the middle plane of the wire) and the rotor is driven by a synchronous motor **M** whose speed is regulated by an inverter.

The rotor set up as illustrated above has a considerable operating flexibility as it is a straightforward task to change some of the parameters that most affect the motion, namely the length, the diameter and the tension of the wire.

As the wire mass is negligible compared to that of the disk, the equations of motion of the disk centre in a fixed reference frame are represented by two differential equations that are ordinary, non-linear and coupled. By making appropriate simplifications and variable substitutions, the equations of motion can be traced back to a pair of coupled Duffing equations.

It is of course well known that the search for non-periodic and chaotic responses in such systems can only be conducted by numerically solving the equations of motion by trial and error, which is very time consuming. For this reason considerable attention has deservedly been paid to a simpler theoretical model with independent equations of motion that do not have any of the original cross coupling terms, so as to get useful information regarding the present investigation.

The simplified equations represent a pair of well studied Duffing equations [4–7, 14, 16]. In particular Ueda [4–7] determined the intervals where the coefficients make the behaviour of the solution non-periodic or chaotic.

The knowledge of these intervals made it possible to establish, with a restricted number of attempts, the values of the parameters and the conditions that determine non-periodic or chaotic motions of this system.

The theoretical investigation indicated that in the presence of the small amounts of damping and unbalance that characterise practical operation, the disk motion can be quasi-periodic but never chaotic.

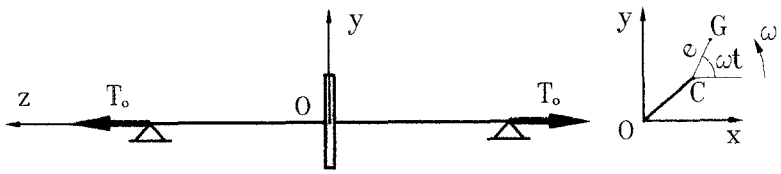

Figure 2. The frame of reference and the reference tension T_0.

The results obtained from the experimental apparatus confirmed this.

2. The Equations of Motion

As the wire mass is negligible in comparison to the disk mass m, the equations of motion of the disk centre **C** in a fixed frame $Oxyz$ (Figure 2), can be written as follows:

$$\begin{cases} m\ddot{x} + (\sigma_e + \sigma_i)\dot{x} + \sigma_i\omega y + f_x(x,y) = me\omega^2 \cos\omega t \\ m\ddot{y} + (\sigma_e + \sigma_i)\dot{y} - \sigma_i\omega x + f_y(x,y) = me\omega^2 \sin\omega t - P \end{cases} \tag{1}$$

with

e	disk eccentricity,
$f_x(x,y)$, $f_y(x,y)$	elastic restoring forces along x and y axes, respectively,
m	disk mass,
P	disk weight,
ω	angular speed of the rotor,
σ_e	external viscous damping coefficient,
σ_i	coefficient of internal damping due to hysteresis.

In equations (1) the external damping is assumed to be viscous and the internal damping, due to the elastic hysteresis of the wire, is approximately considered to be proportional to the angular speed of the wire and to its deflection [1]. Because of the small diameter of the wire, the structural damping can be said to be negligible.

In a generic position (x,y) of **C**, along its plane orbit and under the hypothesis that the wire is perfectly flexible, the restoring force $f(x,y)$ can be expressed as a function of the tension T in the wire (Figure 3):

$$f(x,y) = \sqrt{f_x(x,y)^2 + f_y(x,y)^2} = 2T\sin\vartheta. \tag{2}$$

Assuming the following symbols:

A	area of the wire section $= (\pi/4)d^2$,
d	diameter of wire section,
E	modulus of elasticity,
L	half distance between the supports at the ends of the wire,
L_{IN}	half length of the wire when unstrained,
L_T	half length of the wire under generic tension T,
ΔL	$= L_T - L$,
ε_0	$= (L - L_{IN})/L_{IN}$,
T	tension in the wire $= EA(L_T - L_{IN})/L_{IN} = T_0 + EA(\Delta L/L_{IN})$ $\cong T_0 + EA(\Delta L/L)$,
T_0	reference tension in the wire, corresponding to its horizontal disposition $= EA\varepsilon_0$,

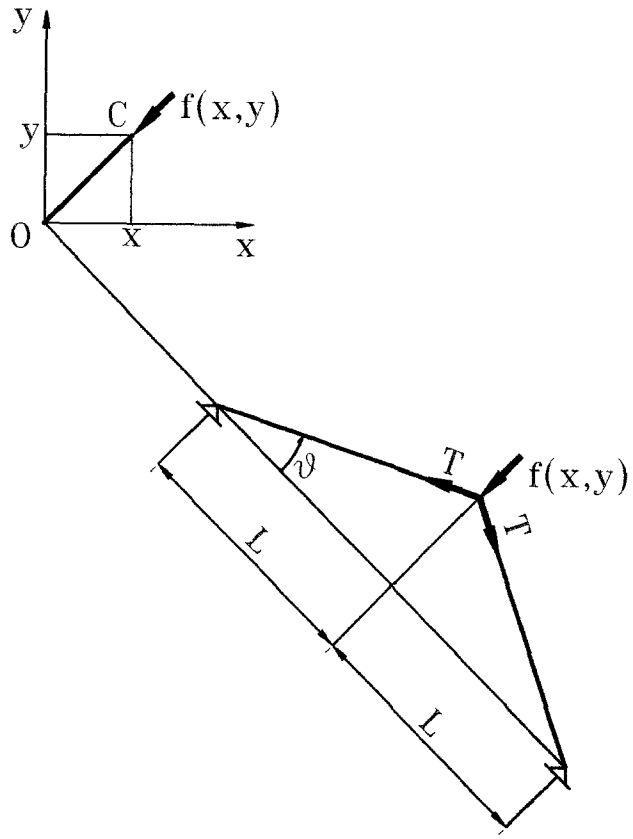

Figure 3. Model for evaluating the elastic restoring force.

the strain in the wire can be calculated by taking into account the following relationship (Figure 3):

$$L^2 + (x^2 + y^2) = L_T^2 = (L + \Delta L)^2 \tag{3}$$

from which it can be inferred that

$$\frac{\Delta L}{L} = \sqrt{1 + \left(\frac{x}{L}\right)^2 + \left(\frac{y}{L}\right)^2} - 1. \tag{4}$$

Because of the relation

$$L_T \sin\vartheta = \sqrt{x^2 + y^2}, \tag{5}$$

we can write

$$\begin{aligned} f(x,y) &= 2T \sin\vartheta \\ &= 2T_0 \left\{ 1 + \frac{EA}{T_0} \left[\sqrt{1 + \left(\frac{x}{L}\right)^2 + \left(\frac{y}{L}\right)^2} - 1 \right] \right\} \frac{\sqrt{(x/L)^2 + (y/L)^2}}{\sqrt{1 + (x/L)^2 + (y/L)^2}}. \end{aligned} \tag{6}$$

Assuming

$$\omega_0^2 = \frac{2T_0}{mL}\,; \quad \frac{\sigma_e}{m} = 2\zeta_e\omega_0; \quad \frac{\sigma_i}{m} = 2\zeta_i\omega_0; \quad \sigma_{cr} = 2\sqrt{\frac{2T_0 m}{L}}\,;$$

$$\zeta_e = \frac{\sigma_e}{\sigma_{cr}}\,; \quad \zeta_i = \frac{\sigma_i}{\sigma_{cr}}\,; \tag{7}$$

$$\bar{u} = \frac{x}{L}\,; \quad \bar{v} = \frac{y}{L}\,, \tag{8}$$

with

ω_0 natural frequency of the linearized system (about the reference horizontal disposition of the wire),
σ_{cr} critical value of the global (internal and external) damping,
ζ_e, ζ_i external and internal fractions of the critical damping,

the equations of motion can be expressed:

$$\begin{cases} \ddot{\bar{u}} + 2(\zeta_e + \zeta i)\omega_0\dot{\bar{u}} + 2\zeta_i\omega_0\omega\bar{v} + \omega_0^2 \\ \qquad \times \left\{1 + \dfrac{EA}{T_0}\left[\sqrt{1+\bar{u}^2+\bar{v}^2} - 1\right]\right\} \dfrac{\bar{u}}{\sqrt{1+\bar{u}^2+\bar{v}^2}} = \dfrac{e}{L}\,\omega^2\cos\omega t \\ \ddot{\bar{v}} + 2(\zeta_e + \zeta_i)\omega_o\dot{\bar{v}} - 2\zeta_i\omega_0\omega\bar{u} + \omega_0^2 \\ \qquad \times \left\{1 + \dfrac{EA}{T_0}\left[\sqrt{1+\bar{u}^2+\bar{v}^2} - 1\right]\right\} \dfrac{\bar{v}}{\sqrt{1+\bar{u}^2+\bar{v}^2}} = \dfrac{e}{L}\,\omega^2\sin\omega t - \dfrac{g}{L}\,. \end{cases} \tag{9}$$

Finally, by means of

$$\omega t = \tau; \qquad r = \frac{\omega}{\omega_0}$$

$$\bar{u}' = \frac{\mathrm{d}\bar{u}}{\mathrm{d}\tau} = \frac{\mathrm{d}\bar{u}}{\mathrm{d}t}\,\frac{\mathrm{d}t}{\mathrm{d}\tau} = \frac{\dot{\bar{u}}}{\omega}\,; \qquad \bar{u}'' = \frac{\mathrm{d}\bar{u}'}{\mathrm{d}\tau} = \frac{\ddot{\bar{u}}}{\omega^2}$$

$$\bar{v}' = \frac{\mathrm{d}\bar{v}}{\mathrm{d}\tau} = \frac{\mathrm{d}\bar{v}}{\mathrm{d}t}\,\frac{\mathrm{d}t}{\mathrm{d}\tau} = \frac{\dot{\bar{v}}}{\omega}\,; \qquad \bar{v}'' = \frac{\mathrm{d}\bar{v}'}{\mathrm{d}\tau} = \frac{\ddot{\bar{v}}}{\omega^2}\,, \tag{10}$$

the equations of motion are given in dimensionless form:

$$\begin{cases} \bar{u}'' + \dfrac{2(\zeta_e + \zeta i)}{r}\,\bar{u}' + \dfrac{2\zeta_i}{r}\,\bar{v} + \dfrac{1}{r^2} \\ \qquad \times \left\{\left(1 - \dfrac{EA}{T_0}\right)(1+\bar{u}^2+\bar{v}^2)^{-1/2} + \dfrac{EA}{T_0}\right\}\bar{u} = \dfrac{e}{L}\cos\tau \\ \bar{v}'' + \dfrac{2(\zeta_e + \zeta i)}{r}\,\bar{v}' - \dfrac{2\zeta_i}{r}\,\bar{u} + \dfrac{1}{r^2} \\ \qquad \times \left\{\left(1 - \dfrac{EA}{T_0}\right)(1+\bar{u}^2+\bar{v}^2)^{-1/2} + \dfrac{EA}{T_0}\right\}\bar{v} = \dfrac{e}{L}\sin\tau - \dfrac{g}{\omega_L^2} \end{cases} \tag{11}$$

representing a system of two differential equations that are ordinary, non-linear and coupled.

3. The Approximate Equations of Motion

Under the hypothesis that the displacements x and y are, in any case, negligible with respect to the half length L of the wire and thus such as to allow the assumption that the dimensionless coordinates u and v are smaller than 1, in equations (11) it can be assumed that

$$(1+\bar{u}^2+\bar{v}^2)^{-1/2} \cong 1-\frac{1}{2}(\bar{u}^2+\bar{v}^2). \tag{12}$$

This gives, with the further assumption $1 - EA/T_0 \cong -EA/T_0$:

$$\begin{cases} \bar{u}'' + \dfrac{2(\zeta_e+\zeta_i)}{r}\bar{u}' + \dfrac{2\zeta_i}{r}\bar{v} + \dfrac{\mu}{r^2}(\bar{u}^2+\bar{v}^2)\bar{u} = \dfrac{e}{L}\cos\tau \\ \bar{v}'' + \dfrac{2(\zeta_e+\zeta_i)}{r}\bar{v}' - \dfrac{2\zeta_i}{r}\bar{u} + \dfrac{\mu}{r^2}(\bar{u}^2+\bar{v}^2)\bar{v} = \dfrac{e}{L}\sin\tau - \dfrac{g}{\omega^2 L}\,. \end{cases} \tag{13}$$

It should be observed that in equations (13) the dimensionless coefficient μ of the non-linear terms in u and v is given by

$$\mu = \frac{EA}{2T_0} \tag{14}$$

and that, for fixed values of E and A (i.e. a piano-wire of fixed diameter is assumed), the value of μ depends on the reference tension T_0.

Keeping constant the values of all the other parameters, the system behaviour is thus affected by the amount of tension T_0. In particular, it is non-linear for small values of T_0 and practically linear when T_0 is high.

Putting

$$\bar{u} = \frac{r}{\sqrt{\mu}}u; \qquad \bar{v} = \frac{r}{\sqrt{\mu}}v, \tag{15}$$

equations (13) can be rewritten:

$$\begin{cases} u'' + \dfrac{2(\zeta_e+\zeta_i)}{r}u' + \dfrac{2\zeta_i}{r}v + u^3 + \left(\dfrac{1}{r^2}+v^2\right)u = \dfrac{\sqrt{\mu}}{r}\dfrac{e}{L}\cos\tau \\ v'' + \dfrac{2(\zeta_e+\zeta_i)}{r}v' - \dfrac{2\zeta_i}{r}u + v^3 + \left(\dfrac{1}{r^2}+u^2\right)v = \dfrac{\sqrt{\mu}}{r}\dfrac{e}{L}\sin\tau - \dfrac{\sqrt{\mu}}{r}\dfrac{g}{\omega^2 L} \end{cases} \tag{16}$$

and assuming

$$\begin{cases} B_0 = \dfrac{\sqrt{\mu}}{r}\dfrac{g}{\omega_L^2} = \dfrac{1}{r^3}\sqrt{\dfrac{EA}{2T_0}}\dfrac{g}{\omega_0^2 L} = \dfrac{1}{2r^3}\sqrt{\dfrac{EA}{2T_0}}\dfrac{P}{T_0} \\ B_1 = \dfrac{\sqrt{\mu}}{r}\dfrac{e}{L} = \dfrac{1}{r}\sqrt{\dfrac{EA}{2T_0}}\dfrac{e}{L} \\ h_e = \dfrac{2\zeta_e}{r}\,; \qquad h_i = \dfrac{2\zeta_i}{r} \end{cases} \tag{17}$$

we can finally write the form

$$\begin{cases} u'' + (h_e+h_i)u' + h_i v + u^3 + \left(\dfrac{1}{r^2}+v^2\right)u = B_1\cos\tau \\ v'' + (h_e+h_i)v' - h_i u + v^3 + \left(\dfrac{1}{r^2}+u^2\right)v = B_1\sin\tau - B_0. \end{cases} \tag{18}$$

By examining equations (18) it can be deduced that the equations of motion for the disk centre – with the approximations (12) – can finally be written as a pair of coupled Duffing equations.

From equations (17) it can be inferred that the values of B_1 and B_0, with the other conditions remaining the same, are proportional to $\sqrt{\mu}$ and that, in particular, the value of B_1 increases with the product $\sqrt{\mu}\, e/L$.

Finally, according to (7) and (14), and assuming that all other conditions are kept constant, we can conclude that when T_0 decreases the system not only becomes less linear, but also more damped, in the sense that the values of μ and of the ζ_e and ζ_i ratios increase.

4. Non-Periodic Motions of the Disk Center

The theoretical search for non-periodic solutions of the set of equations like (18) through analytical approaches is quite involved (e.g., see in [22] the treatment of secondary resonances in Multi-Degree-of-Freedom systems with analytical methods) or not possible, and can be sometimes carried out provided that some stiff approximations are introduced. Thus we go on with the theoretical analysis of the rotor system by numerically solving the equations (18) with trial and error techniques involving the parameters r, B_0, B_1, ζ_e and ζ_i.

In order to reduce the number of attempts needed to determine non-periodic motions of the disk centre, we proceeded as follows.

Taking equations (18) once again into examination, it can be observed that, if the coupling terms are neglected, the same equations become

$$u'' + (h_e + h_i)u' + \frac{1}{r^2}\, u + u^3 = B_1 \cos\tau \tag{19}$$

$$v'' + (h_e + h_i)v' + \frac{1}{r^2}\, v + v^3 = B_1 \sin\tau - B_0 \tag{20}$$

and further, when $r \gg 1$:

$$u'' + (h_e + h_i)u' + u^3 = B_1 \cos\tau \tag{21}$$

$$v'' + (h_e + h_i)v' + v^3 = B_1 \sin\tau - B_0. \tag{22}$$

Equations (21) and (22) represent a pair of well-studied Duffing's equations, for which the values of the parameters h_i, h_e, B_0, B_1, that give non-periodic solutions were determined using a trial and error procedure [4–7]. Some outstanding results regarding equations similar to (19–22) are reported in [9, 10, 14, 16, 17, 24].

As far as the above is concerned, it must be observed that the motion described by equation (21) shows chaotic evolutions for rather high values of the parameter B_1 [5] that correspond, in respect of (16), to high values of the product $\sqrt{\mu}\, e/L$, i.e. high values of the coefficient of non-linearity μ and/or of the rotor static unbalance "e". It must be pointed out that these conditions do not take place in the practical case of rotors that are supported on roller bearings, which generally exhibit small values of non-linearity and residual unbalances (after balancing procedures).

Vice versa, the motion described with equation (22), becomes chaotic for

$$h = h_e + h_i = 0.05; \quad B_0 = 0.045; \quad B_1 = 0.16 \tag{23}$$

$$h = h_e + h_i = 0.05; \quad B_0 = 0.03; \quad B_1 = 0.16 \tag{24}$$

and the value of B_1 in (23) and (24) is quite small.

Starting numerical trials with the values in (23) and the approximate equations in (18), it was possible to determine – with a limited number of attempts – the values of the parameters r, ζ_e, ζ_i, B_0, B_1, that make the motions described by these equations non-periodic.

Many sets of trials were carried out; in each one the values of ζ_e, ζ_i and r, were kept constant while varying the values of B_0 and B_1 in the ranges:

$$0.02 \leq B_0 \leq 0.08; \qquad 0.02 \leq B_1 \leq 0.24. \tag{25}$$

In the above corresponding intervals, the values of B_0 and B_1 were taken in steps of 0.01 and 0.02, respectively; 84 numerical integrations were performed for each set of trials and, because there were adopted nine different sets of ζ_e ζ_i and r, the theoretical investigation needed 756 integrations in all.

For each integration of the equations of motion (18) the kind of solution was inferred mainly by examining the orbits of the disk centre.

It is worth pointing out that where non-periodic solutions of equations (18) were detected, some further checks were made by integrating the equations (11), with different values of μ: these checks made it possible to infer that even in chaotic conditions equations (18) give results that do not essentially differ from those obtained with the exact equations (11).

5. Results of the Theoretical Investigation

As an example of the theoretical investigation carried out, Figures 4a–c show the results of three sets of trials, referring to the following values of the parameters h_i, h_e and r, respectively:

Figure 4a:	$r = 3.5;$	$2\zeta_e/r = h_e = 0.05;$	$2\zeta_i/r = h_i = 0$
Figure 4b:	$r = 3.5;$	$2\zeta_e/r = h_e = 0;$	$2\zeta_i/r = h_i = 0.05$
Figure 4c:	$r = 3.5;$	$2\zeta_e/r = h_e = 0.005;$	$2\zeta_i/r = h_i = 0.005.$

A number of points have been fixed in the B_1B_0 coordinate plane (Figures 4a–c) and a suitable graphic symbol indicates for each point the relative kind of motion that was described by the disk centre as a result of the numerical integration.

The results of the theoretical investigation can be summarized as follows:

(1) In the absence of internal damping ($h_i = 0$), with quite high values of external damping ($h_e = 0.05$) and with the values of r, B_0 and B_1 considered here, the motion of the rotor, as described by equations (18), is quasi-periodic (Figure 4a).

The solution of equations (18) is chaotic for values of B_0 and B_1 that are not very different from the ones that make the solution of Duffing's equation (22) chaotic.

As an example of a chaotic solution, Figure 5 illustrates some diagrams referring to the following parameter values:

$$r = 3.5; \quad h_e = 0.05; \quad h_i = 0; \quad B_0 = 0.045; \quad B_1 = 0.179. \tag{26}$$

This figure shows:

(a), (b): the diagrams $u(\tau)$ and $v(\tau)$, with $12765 < \tau < 12915$ rad, corresponding to about 20 cycles of driving force, after the initial 2000 cycles, such as to extinguish the

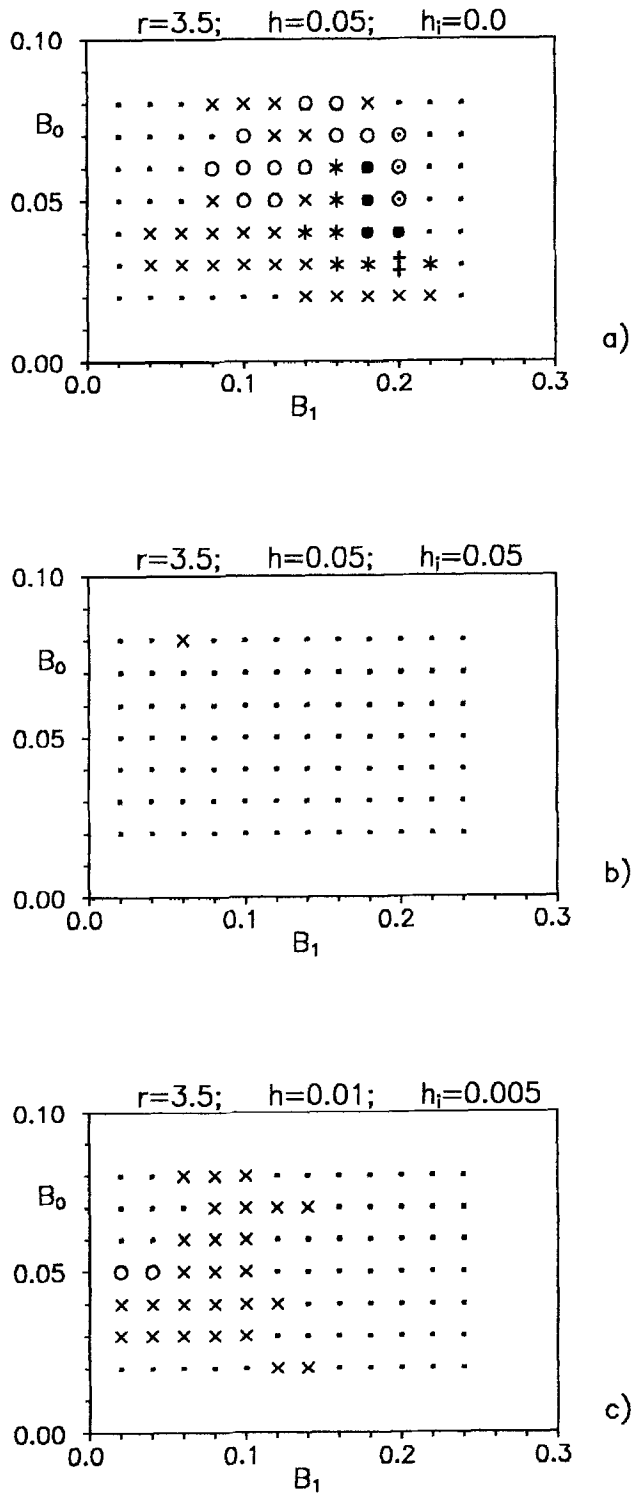

Figure 4. Different types of motion obtained as numerical solutions of the equations (18), varying B_1 and B_0, with $r = 3.5$ and three different combinations of internal and external damping: (a) $h = 0.05$, $h_i = 0.0$; (b) $h = 0.05$, $h_i = 0.05$; (c) $h = 0.01$, $h_i = 0.005$. Symbols: •: synchronous orbit with period $\mathbf{T}_s = 2\pi/\omega$; ×: periodic orbit with period $\mathbf{T} = 2\mathbf{T}_s$; ∗: periodic orbit with period $\mathbf{T} = 4\mathbf{T}_s$; ‡: periodic orbit with period $\mathbf{T} = 8\mathbf{T}_s$, ⊙: synchronous orbit after a chaotic transient behaviour; ○: quasi-periodic orbit, ●: chaotic behaviour.

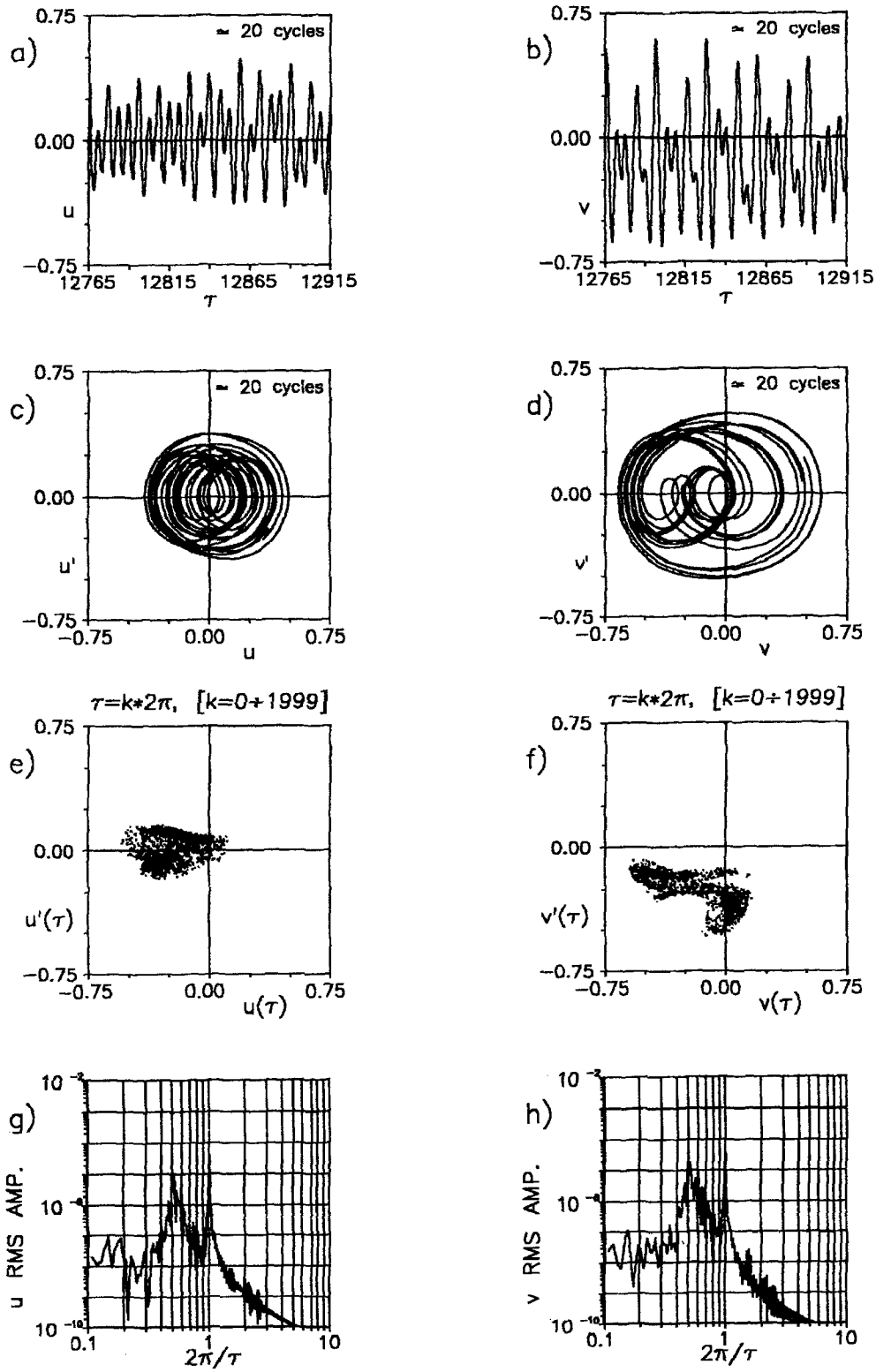

Figure 5. Results of numerical integration of the equations (18) with $r = 3.5$, $h_e = 0.05$, $h_i = 0$, $B_0 = 0.045$, and $B_1 = 0.179$: (a) u motion *versus* τ; (b) v motion *versus* τ; (c) orbits in the uu' phase plane; (d) orbits in the vv' phase plane; (e) Poincaré section projected onto the uu' phase plane; (f) Poincaré section projected onto the vv' phase plane; (g) RMS amplitude spectrum of the $u(\tau)$ motion; (h) RMS amplitude spectrum of the $v(\tau)$ motion.

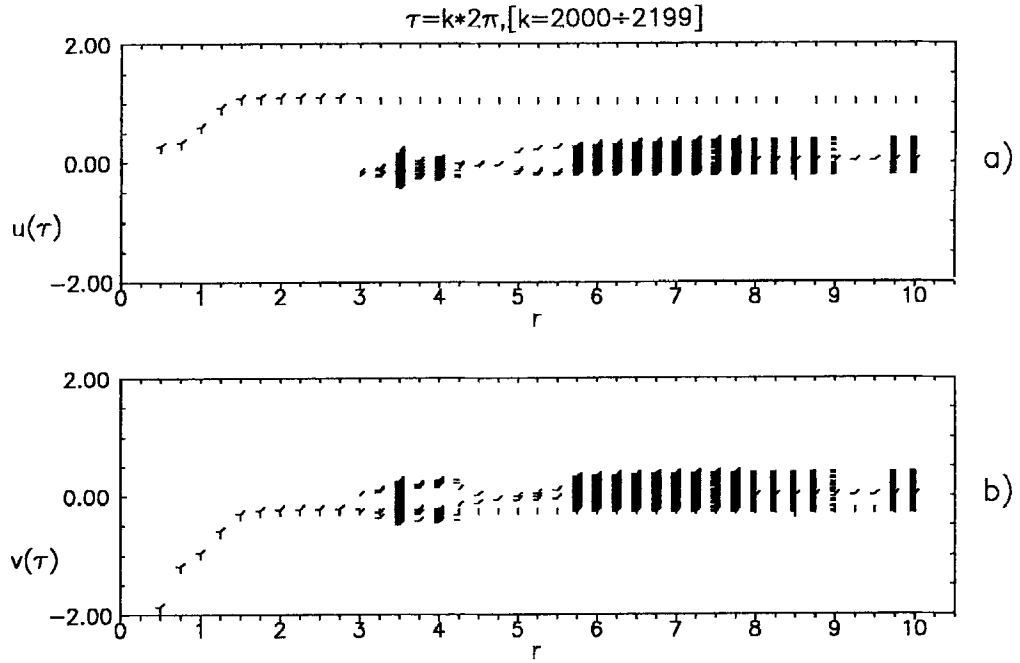

Figure 6. Bifurcation diagrams obtained varying r and projecting Poincaré sections onto: (a) u axis; (b) v axis. Symbols: /: solutions with set S1 of initial conditions; –: solutions with set S2 of initial conditions; |: solutions with set S3 of initial conditions.

starting transient;
(c), (d): the phase diagrams $u'(u)$ and $v'(v)$, relating to the same cycles;
(e), (f): the projections of the Poincaré section onto the phase planes uu' and vv' that are relative to 2000 cycles of the driving force, recorded after the initial 2000 cycles;
(g), (h): the RMS amplitude spectra of the $u(\tau)$ and $v(\tau)$ motions.

The diagrams in Figure 5 make it possible to infer:

(1) from 5a and 5b the non-periodic behaviour of $u(\tau)$ and $v(\tau)$;
(2) from 5c and 5d the apparent chaotic nature of the same motions;
(3) from 5e and 5f the difference between the two projections of the Poincaré section onto the respective phase planes; in particular the projection of the Poincaré section in the phase plane vv', depicted in Figure 5f, appear with a fractal structure, while the projection onto the phase plane uu' exhibits a different shape;
(4) from 5g and 5h the presence of a broad band with irregular fluctuations of frequency components, as a further indication of the chaotic behaviour.

Two bifurcation diagrams, referring to the $u(\tau)$ and $v(\tau)$ motions, are reported in Figures 6a and 6b, respectively.

In these diagrams the $u(\tau)$ and $v(\tau)$ solutions of (18), taken stroboscopically as projections of the Poincaré section onto the u and v axes, respectively, are reported varying r in the interval $0.5 \leq r \leq 10$, at a step equal to 0.25. For each value of r, the diagrams report together the solutions obtained starting the numerical integration with three different sets of initial conditions. An adequate number of points (200 in the case of non-periodic behaviour) was

recorded after the first 2000 cycles, for each integration. The three sets of initial conditions that were adopted are

$$\begin{array}{llll} \text{S1:} & u(0)=0 & v(0)=0 & u'(0)=0 \quad v'(0)=0 \\ \text{S2:} & u(0)=0 & v(0)=0 & u'(0)=0.3 \quad v'(0)=-0.3 \\ \text{S3:} & u(0)=-0.1 & v(0)=0.1 & u'(0)=-3.0 \quad v'(0)=0. \end{array}$$

It must be pointed out that the values of $h = h_i + h_e$, B_0 and B_1, in equations (18), (19) and (20), vary with r, according to (17) and (26) in respect of the following relationships:

$$h(r) = 0.05 \cdot 3.5/r; \quad B_0(r) = 0.045 \cdot (3.5/r)^3; \quad B_1 = 0.179 \cdot 3.5/r. \tag{27}$$

With the S3 set of initial conditions, the motion is synchronous for all the values of r fixed in the range $0.5 \leq r \leq 10$, with the exception of $r = 8.5$ that makes the solution quasi-periodic.

The other two sets S1 and S2 give in turn, for each fixed value of r in the range $0.5 \leq r \leq 2.75$, the same synchronous solutions obtained with S3.

For $r = 3$, the motion obtained with S1, is subharmonic with $2\mathbf{T}_s$ period; the solution obtained with S2 is still synchronous and coinciding with the response given by the S3 set.

In almost all the interval $3.25 \leq r \leq 7.75$, both S1 and S2 determine the same following solutions, that are different from the synchronous motions relating to S3:

- subharmonic, with period $\mathbf{T} = 4\mathbf{T}_s$, with $r = 3.25$;
- chaotic, for $r = 3.5$;
- subharmonic, with period $\mathbf{T} = 8\mathbf{T}_s$, for $r = 3.75$;
- chaotic, for $r = 4$, with the points of the $v(\tau)$ diagram gathering densely on two segments;
- subharmonic, with period $\mathbf{T} = 2\mathbf{T}_s$, for $r = 4.5$;
- synchronous, for $r = 4.75$;
- subharmonic, with period $\mathbf{T} = 3\mathbf{T}_s$, with r in the interval $5 \leq r \leq 5.5$;
- quasi-periodic, in the range $5.75 \leq r \leq 7.75$.

On the contrary, the responses obtained with S1 and S2 are distinct when $r = 4.25$: the Poincaré sections are made of 2 points when the set S1 is adopted, and 4 points with the set S2.

With the r values fixed in the range $8 \leq r \leq 10$, S1 gives synchronous responses that are different from the synchronous solutions determined in this zone with S3.

On the other hand, when the set S2 is adopted in the same interval of r, quasi-periodic solutions are determined, with the exception of the synchronous motions obtained with $r = 9.25$ and 9.5, that coincide with the ones given respectively by S1. The quasi-periodic response obtained with $r = 8.5$ is the same obtained when the set S3 is adopted.

A suitable number of chaotic orbits of the disk centre, in the uv coordinate plane, obtained after the first 2000 revolutions of the system, have been plotted in sequential groups of three in Figure 7. This figure also reports and numbers the points that correspond to the projection of the Poincaré section onto the uv coordinate plane.

Finally, Figure 8 shows the Lyapunov exponents (computed as indicated in [12]) relative to the same motion.

(2) If the prevailing damping is the one that corresponds to the elastic hysteresis of the shaft material ($\dot{h}_e = 0$, $h_i = 0.05$), for the same values already given in (1) to the remaining

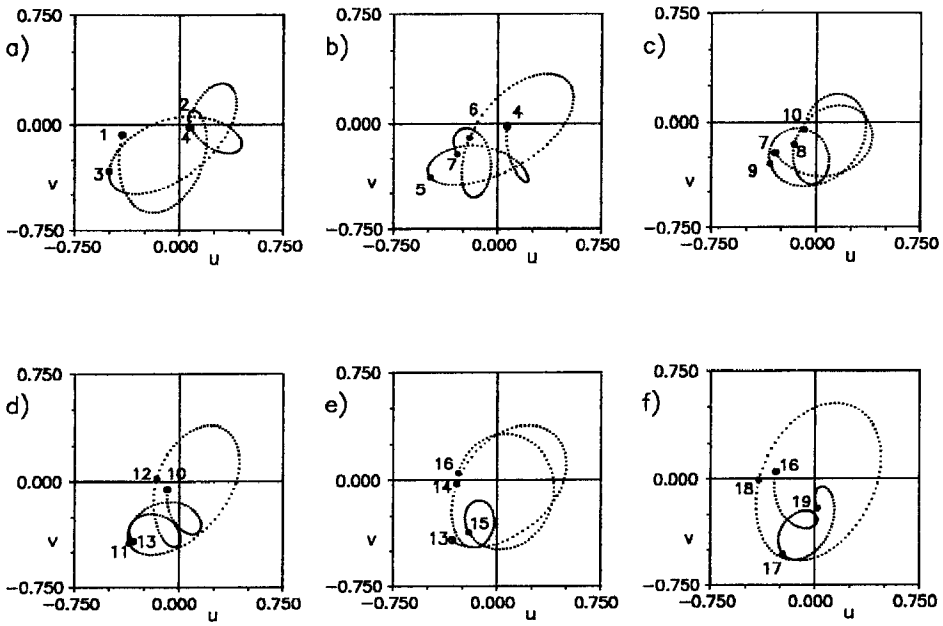

Figure 7. Orbits of the disk centre in the uv plane, illustrated in sequential plots. Equations (18) were numerically integrated with $r = 3.5$, $h_e = 0.05$, $h_i = 0$, $B_0 = 0.045$, and $B_1 = 0.179$.

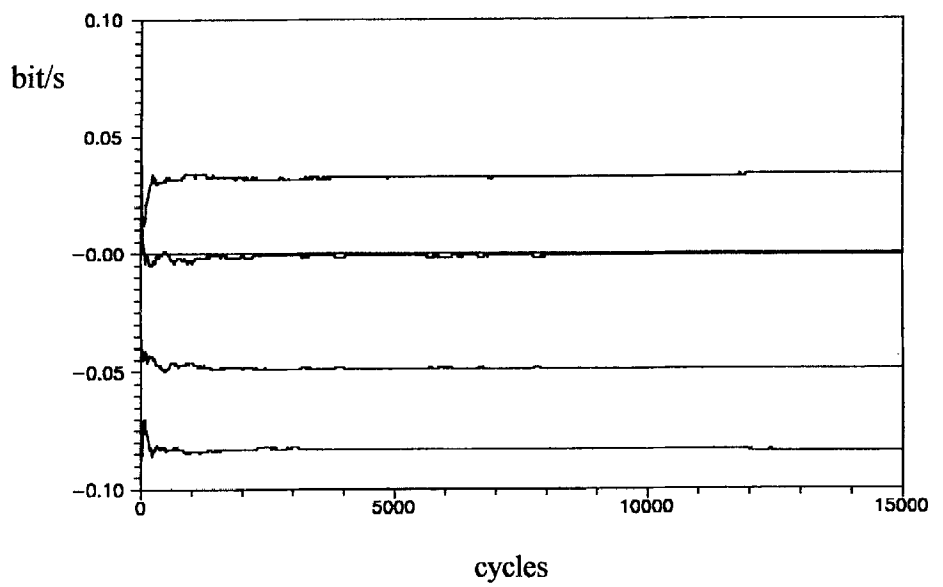

Figure 8. Lyapunov exponents with $r = 3.5$, $h_e = 0.05$, $h_i = 0$, $B_0 = 0.045$, and $B_1 = 0.179$.

parameters r, B_0 and B_1, the motion of the rotor is always periodic and generally synchronous (see Figure 4b).

(3) In the presence of damping actions that are relatively small, but of either type (external or internal), the disk centre motion is generally periodic and at most quasi-periodic, for limited ranges of the parameter values, but it is never chaotic (Figure 4c).

As an example of the quasi-periodic motions that occur in these conditions, Figure 9 reports the diagrams obtained for the following parameter values:

$$r = 2.16; \quad h_e = 0.0015; \quad h_i = 0.002; \quad B_0 = 0.029; \quad B_1 = 0.02. \tag{28}$$

The above diagrams have been collected in Figure 9 with the same layout of Figure 5.

In Figure 10 the orbits of the disk centre and the related projection of the Poincaré section onto the same coordinate plane have been plotted.

6. The Experimental Model

The experimental model corresponds to the schematic drawing in Figure 1.

The brass disk **D** is clamped to the piano wire by means of the element **S** (see Figure 11); this clamp, made of two equal parts (that are symmetrical along an axial plane and are also made of brass) is axially drilled with a bore that is slightly less than the wire diameter; it has a cylindrical shape that ends in a truncated cone at either end and is clamped onto the wire by means of two steel screws **V**.

Both sides of the disk rim have a separate ring that is clamped onto the disk itself by means of a securing screw.

In order to obtain a fixed value for disk unbalance, each ring presents four holes with a 6.5 mm diameter: adjusting the relative angular position of the two rings, it is possible to give a prefixed value to the mass centre nominal eccentricity e in the interval: $0.0 \leq e \leq 1.1$ mm.

The disk mass, complete with rings, clamping element and the relative screws, is 0.4 kg.

Figure 12 shows an illustration of one of the two supports at the ends of the rotor.

The wire clamping at each ball bearing in the relative rotor support is obtained once again by means of a clamping element **S** consisting of two pieces.

Once the wire is clamped by means of the screw **V**, it becomes integral with the bush **b** that rotates with the inner ring of the axial ball bearing.

It is now possible to give the wire a fixed tension T, by rotating the hand ring nut **M** of each of the two supports: by rotating the ring nut (Figure 12) the bush **b** slides inside the bearing internal ring and gives the wire the assigned axial load.

The actual tension T is greater than the reference tension T_0 that would affect the wire in static conditions with no disk weight. The measurement of the static deflection due to the disk weight was adopted to check the tensions T and T_0.

The rotor is driven by an asynchronous motor that is powered at an adjustable frequency by means of an inverter.

Figure 13 shows a photograph of the experimental apparatus.

The high flexibility of the wire during operation means that the orbits described by the disk centre can be observed directly and recorded with a video camera-based system. The orbits were further identified using two capacitive transducers fitted in orthogonal mutual mountings at the end of the wire, near one of the supports. In this zone the size of the orbits is small enough for the operation of the type of transducer chosen.

In this connection, it must be observed that the orbits described by the various sections of the wire are similar if the wire is assumed to be perfectly flexible and to have a negligible mass.

In order to record the orbits with the highest possible accuracy, a small aluminium disk 10 mm in diameter, 5 mm long and with a mass of $8 \cdot 10^{-4}$ kg, was fitted on the wire in the measuring plane.

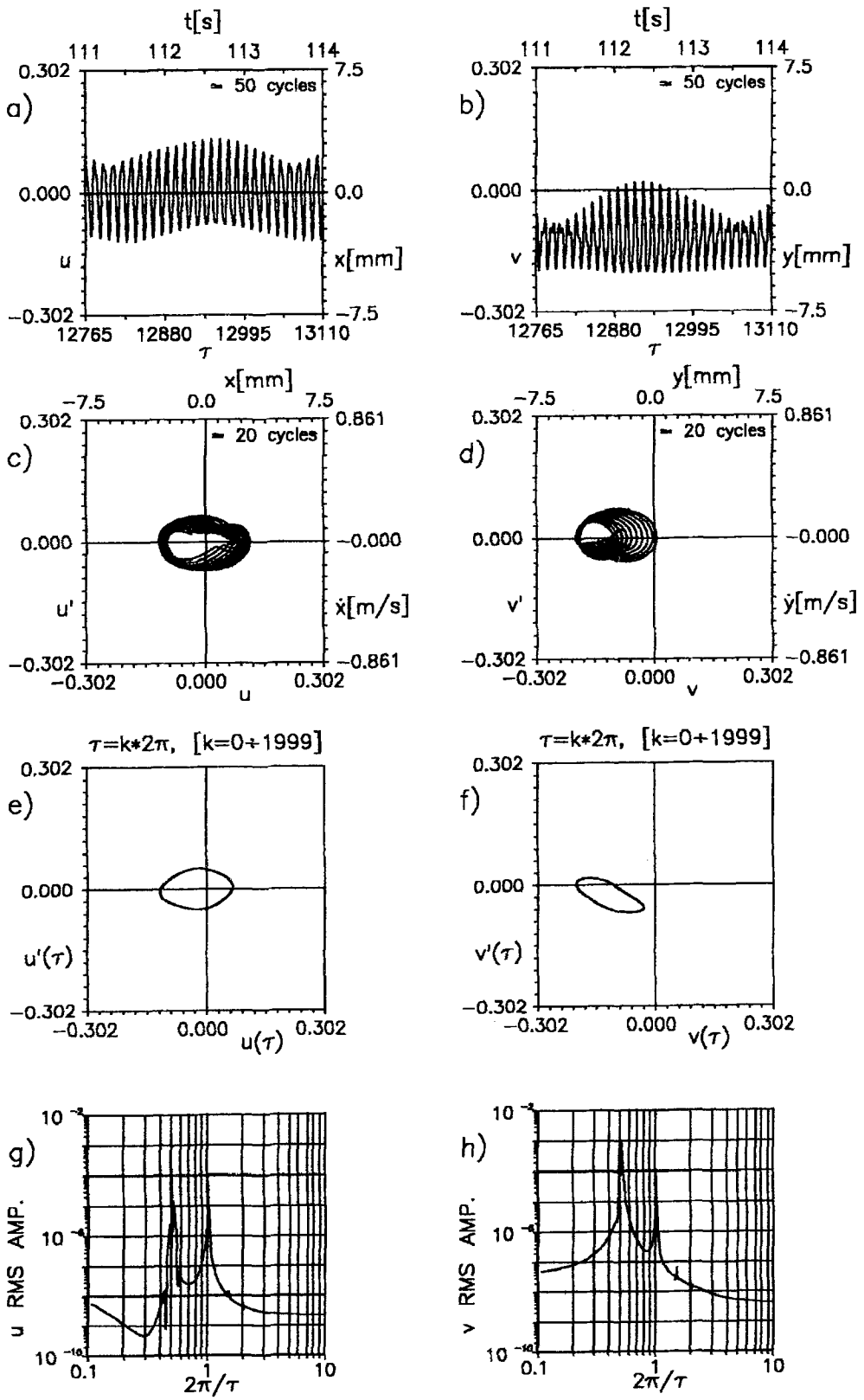

Figure 9. Results of numerical integration of the equations (18) with $\tau = 2.16$, $h_e = 0.0015$, $h_i = 0.002$, $B_0 = 0.029$, and $B_1 = 0.02$: (a) u motion *versus* τ; (b) v motion *versus* τ; (c) orbits in the uu' phase plane; (d) orbits in the vv' phase plane; (e) Poincaré section projected onto the uu' phase plane; (f) Poincaré section projected onto the vv' phase plane; (g) RMS amplitude spectrum of the $u(\tau)$ motion; (h) RMS amplitude spectrum of the $v(\tau)$ motion.

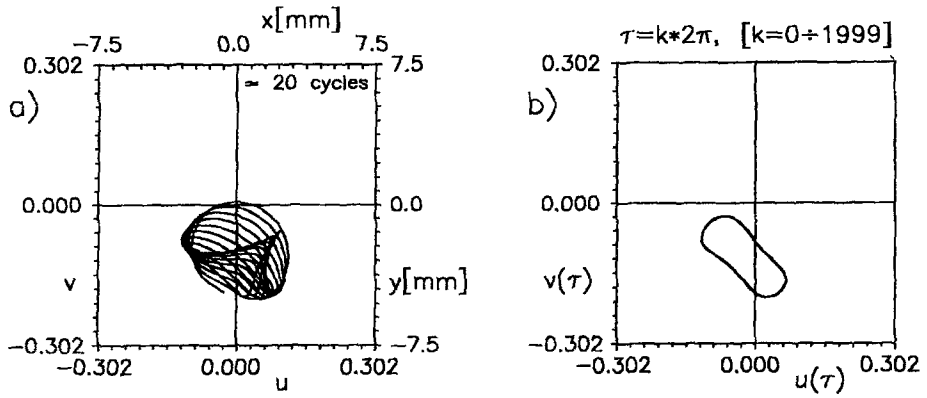

Figure 10. (a) Orbits of the disk centre in the uv plane; (b) Poincaré section projected onto the uv coordinate plane. Equations (18) were numerically integrated with $r = 2.16$, $h_e = 0.0015$, $h_i = 0.002$, $B_0 = 0.029$, and $B_1 = 0.02$.

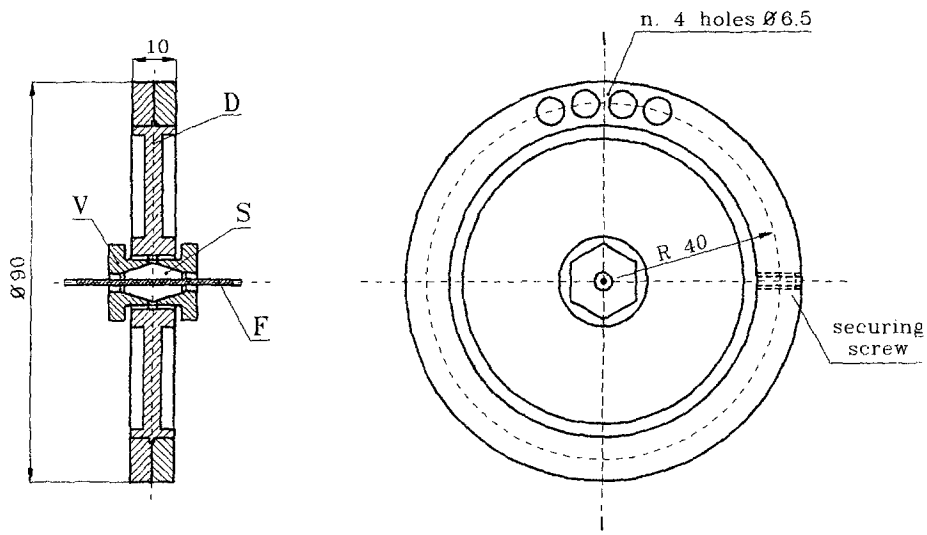

Figure 11. The disk with its clamp and the rings for adjusting the unbalance.

The capacitive transducers were connected to a DISA converter; the output analogic signals from the converter were sent to a data acquisition board (Bakker Electronics mod.490) and the digital signals were recorded and processed with a PC.

The signals can be filtered and derived by means of known numerical algorithms.

In order to obtain the Poincaré sections, a pulse signal, obtained from an electromagnetic transducer facing a disc integral with the rotor and provided with a reference mark shaped as a sharp edge, is recorded together with the signals from the capacitive transducers.

The pulse signal thus obtained can be phased with the disk unbalance.

7. Experimental Results

The experimental system was set up in the following way:

$$L = 0.3\ \text{m}, \quad d = 1.2\ \text{mm}, \quad m = 0.4\ \text{kg}. \tag{29}$$

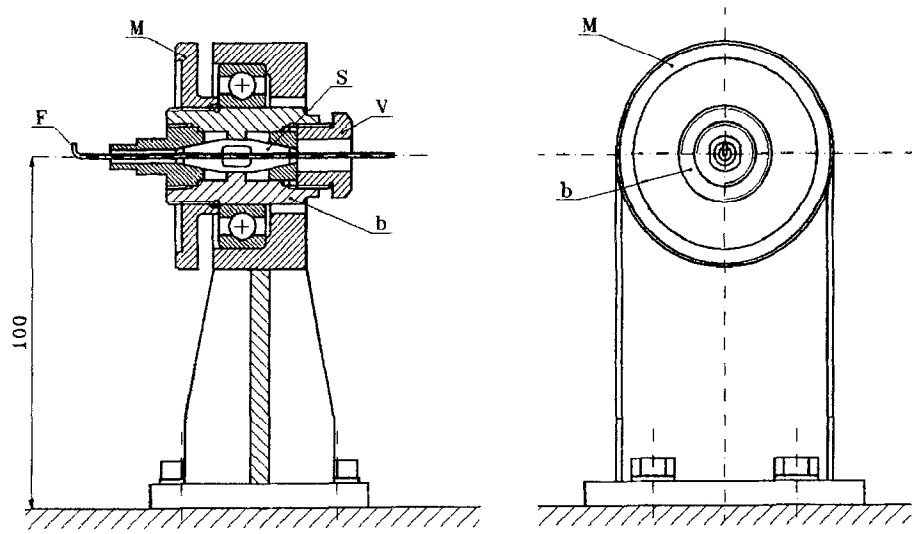

Figure 12. The support system at the ends of the wire.

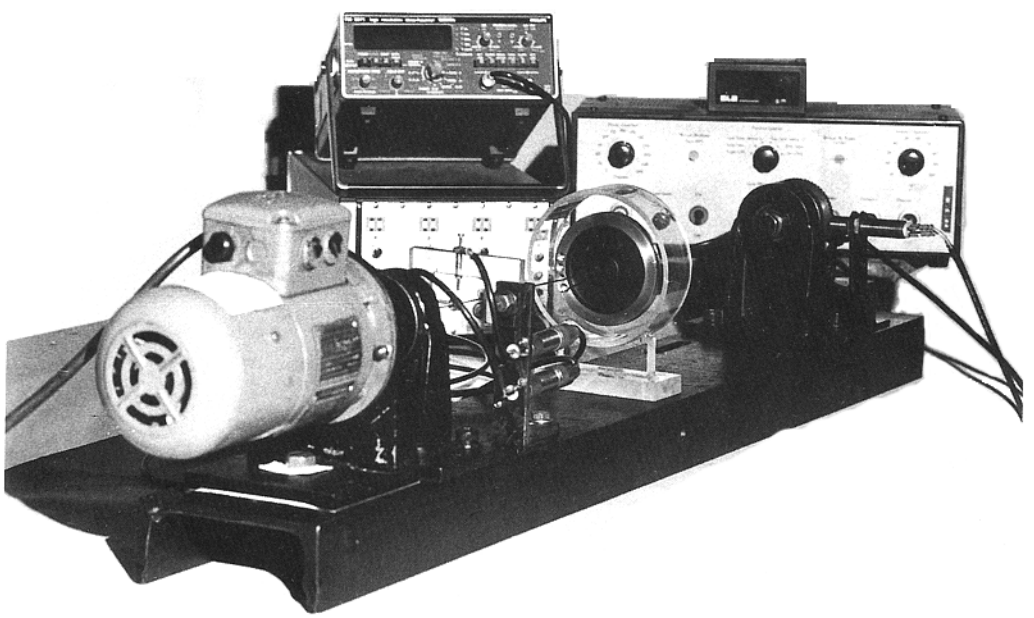

Figure 13. The experimental apparatus.

For the system thus arranged the damping was experimentally measured by recording the free oscillations $x(t)$ and $y(t)$ excited by an initial displacement, for $\omega = 0$ and some values of the reference tension T_0.

The most evident results of this part of the experimental investigation can be reported as follows:

(a) The free oscillations $x(t)$ and $y(t)$ of the disk centre, in addition to the fundamental frequency, show harmonics whose frequencies are not exactly multiples of the fundamental one;

(b) the free oscillations $x(t)$ and $y(t)$ of the disk centre exhibit beat phenomena that are not always related to the coupling phenomena of the above motions; this is more evident when the free oscillation is excited giving an initial displacement in the horizontal direction x;
(c) in these events the beats seem to be generated by the presence, in the x motion, of harmonics with frequencies that are higher than the fundamental one, but not exactly multiples of it;
(d) the mean ζ values, indicated as ζ_{med} and computed with the formulae referred to the viscous damping hypotheses

$$\zeta_i = \frac{1}{2\pi k} \ln \frac{a_{1,i}}{a_{k+1,i}}$$

$$\zeta_{\text{med}} = \frac{1}{n} \sum_{i=1}^{n} \zeta_i \tag{30}$$

with $a_{j,i}$ = width of the j-th displacement of the oscillation detected for computing the ζ_i value; k = number of the cycles adopted for computing the i-th logarithmic decrement and the ζ_i ratio; n = number of the ζ_i values computed in order to determine ζ_{med}, turned out to be very small and of the order of 10^{-3}.
(e) in particular, $\zeta_{\text{med}} = 2.5 \cdot 10^{-3}$ was measured for the horizontal motion with a prevailing horizontal initial displacement, and $\zeta_{\text{med}} = 1.5 \cdot 10^{-3}$ was obtained for the vertical motion excited by a prevailing vertical initial displacement.

Many tests were carried out on the experimental system, varying the angular speed ω, with different assigned values of the reference tension T_0 and of the disk unbalance. In none of these tests were chaotic motions of the disk observed, as inferred from the theoretical results referred to low damping values.

On the other hand, quasi-periodic motions were observed with relatively small disk unbalances, and giving T_0 several different values: this result also agrees with the theoretical results.

As an example, Figure 14 illustrates the diagrams relating to the following test conditions:

$$T_0 = 170\,\text{N}; \quad e = 0.5\,\text{mm}; \quad \omega = 115.2\,\text{rad/s}. \tag{31}$$

It must be observed that, according to (17), the values given in (29) and (31) correspond to the following values of B_0, B_1, ω_0 and r:

$$r = 2.16; \quad B_0 = 0.029; \quad B_1 = 0.02; \quad \omega_0 = 53.3\,\text{rad/s}. \tag{32}$$

Because of the equality between the values of B_0, B_1 and r in (32) and the corresponding ones that appear in (28), the comparison between the theoretical diagrams of Figure 9 and the experimental plots in Figure 14 is significant, at least from a qualitative point of view, since the experimental values of h_e and h_i, which are not expressed in (32), are of the same magnitude as those that appear in (28), in accordance with the comments in the beginning of this paragraph.

In order to enable a simple comparison of the theoretical results in Figure 9 and the experimental ones in Figure 14, dimensional axes x, y, t, $\dot{x}$, $\dot{y}$ have been reported in Figure 9 together with the corresponding dimensionless axes u, v, τ, u' and v'.

The conversion factors can be easily obtained from equations (8) and (15):

$$x/L = y/L = ru/\sqrt{\mu}$$

$$\dot{x}/L = \dot{y}/L = r\dot{u}/\sqrt{\mu} = ru'\omega/\sqrt{\mu}.$$

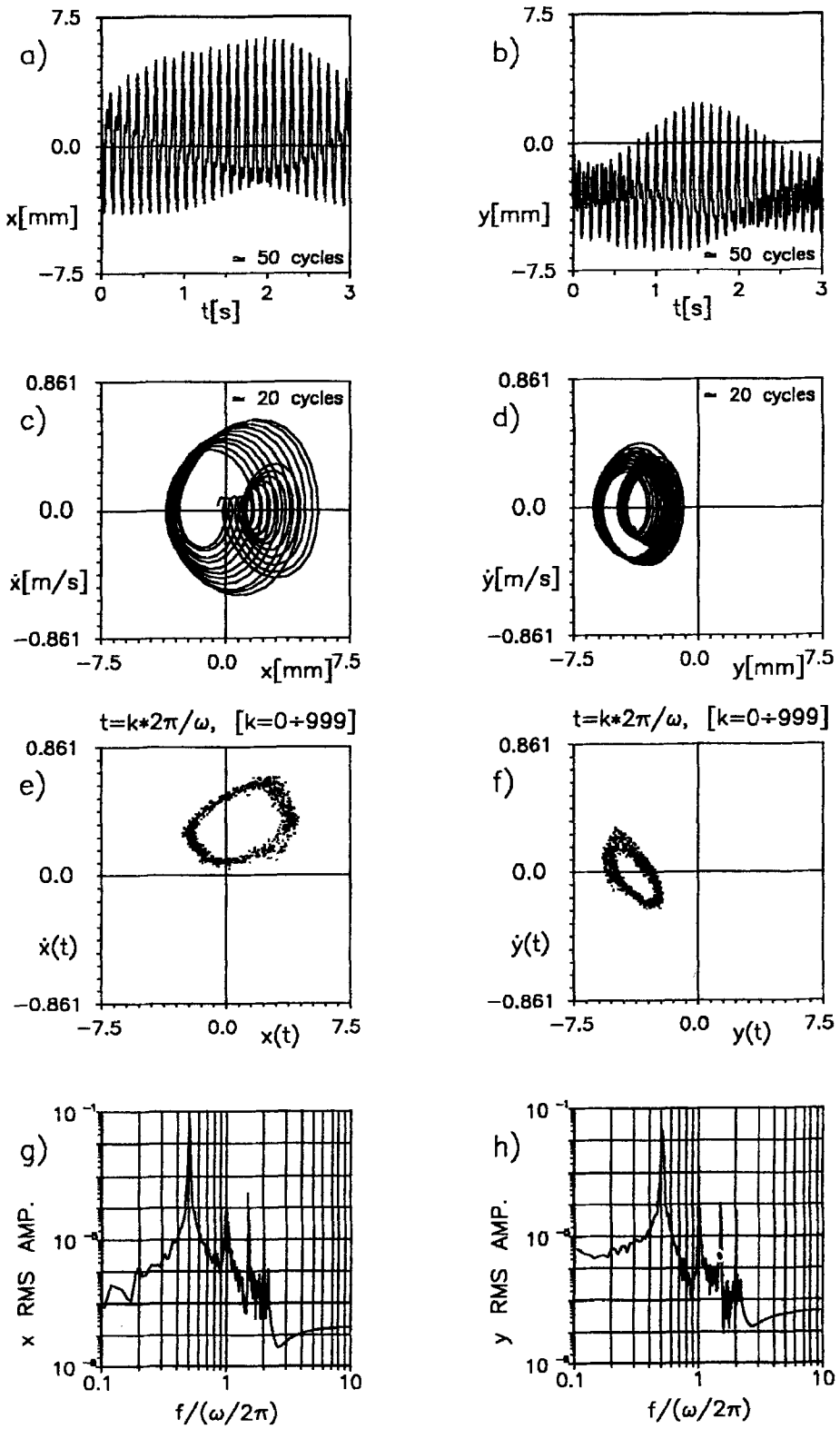

Figure 14. Experimental results obtained with the values of the parameters given by (7.2) and (7.3): (a) x motion *versus* t; y motion *versus* t; (c) orbits in the $x\dot{x}$ phase plane; (d) orbits in the $y\dot{y}$ phase plane; (e) Poincaré section projected onto the $x\dot{x}$ phase plane; (f) Poincaré section projected onto the $y\dot{y}$ phase plane; (g) RMS amplitude spectrum of the x motion; (h) RMS amplitude spectrum of the y motion.

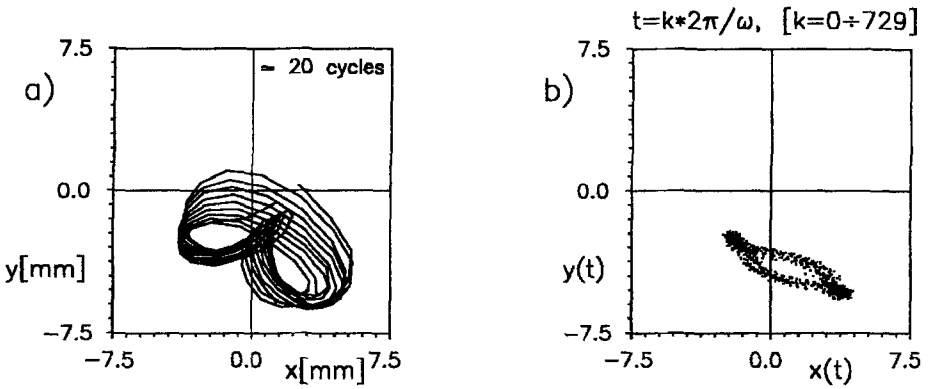

Figure 15. (a) Experimental orbits of the disk centre in the xy plane; (b) Poincaré section projected onto the xy coordinate plane.

Taking into account the following values that have been fixed for the experimental rotor:

$$L = 0.3 \text{ m}; \quad \sqrt{\mu} = \sqrt{\frac{EA}{2T_0}} = 26.177; \quad r = 2.16$$

the conversion factors can be deduced:

$$u/x = 40.4 \text{ m}^{-1}; \quad u'/\dot{x} = v'/\dot{y} = 0.351 \text{ sm}^{-1}.$$

Taking into account these scale factors and the calibration factor of the transducers, the diagrams that correspond in Figures 9 and 14 have been plotted on the same scale, in order to facilitate the relative comparison.

From the comparison between the homologous diagrams in the above figures, it can be pointed out that the experimental results are in good agreement with the theoretical ones, confirming the quasi-periodic nature of the disk centre motion, even if $x(t)$ and $y(t)$ motions exhibit higher amplitudes than the corresponding theoretical ones.

In particular, it can be inferred that:

- the phase diagrams $\dot{x}(x)$ and $\dot{y}(y)$ obtained from the experiments are not so different from the theoretical ones;
- taking into account the unavoidable dispersion of the experimentally obtained Poincaré sections, the projections onto the phase planes $x\dot{x}$ and $y\dot{y}$ confirm the quasi-periodicity of the theoretically obtained motions;
- the comparison between the theoretical power spectra and the experimental ones points out that a 1/2 order harmonic component, with power that is greater than the fundamental, appears in both the theoretically obtained and the experimentally observed motions.

In Figure 15 the experimental trajectories described by the disk centre have been reported in x, y coordinates together with the related projection of the Poincaré section: these plots can be compared with the corresponding ones in Figure 7.

8. Conclusions

The conditions that make the motion of a rotor fitted with ball bearings either non-periodic or chaotic in the presence of non-linear elastic forces have been examined.

The rotor is made of a thin disk and the system presents an axis of rotation that is horizontal and symmetrical along a plane that is normal to the axis of rotation, taken in the middle of the wire shaft.

The differential equations relative to the disk centre motion of the Jeffcott rotor thus arranged are ordinary, non-linear and coupled.

The research included both a theoretical and an experimental investigation.

The theoretical investigation of the non-periodic rotor motions was carried out using a number of numerical trials and integrating the equations of motion with a 4th order Runge–Kutta routine with adaptive stepsize control.

The results of the theoretical investigation can be summarized as follows:

(1) With no internal damping ($h_i = 0$) and relatively high values of the external damping ($h_e = 0.05$) the motion of the rotor is often quasi-periodic (Figure 4a), for the values of r, B_0 and B_1 that have been selected for the present analysis.
For values of B_0 and B_1 that are not so different from those that make the solution of Duffing's equation (22) chaotic, the rotor motion described by (18), is chaotic.

(2) If the prevailing damping is the one that is due to the elastic hysteresis of the shaft material ($h_e = 0$, $h_i = 0.05$) the system shows only periodic, and generally synchronous behaviours (see Figure 4b), varying r, B_0 and B_1 in the same intervals of values selected in (1), respectively.

(3) For damping values that are fairly small, but of either external and internal origin, the disk centre motion is generally periodic, achieving at most a quasi-periodic character for a limited number of different values assigned to the parameters, but never a chaotic one (see Figure 4c).

The results obtained in a large number of experimental tests and the agreement with the theoretical data point out that the small damping values that affect the real system make it impossible to obtain chaotic disk motions by varying the reference tension T_0 and the rotor unbalance.

On the other hand, it was possible to obtain quasi-periodic evolutions for several assigned values of the tension T_0 and with relatively small values of the disk unbalance: this result also substantially agrees with the theoretical expectations.

Symbols

A	section area of the wire
B_0, B_1	coefficients in the Duffing equation
d	diameter of the wire
e	disk eccentricity
E	modulus of elasticity
f	frequency
$f(x, y)$	$= \sqrt{f_x^2 + f_y^2} = 2T \sin\vartheta$: elastic restoring force due to the wire
$f_x(x, y)$, $f_y(x, y)$	elastic restoring forces along x and y axes, respectively
h	$2\zeta/r$
h_e	$2\zeta_e/r$
h_i	$2\zeta_i/r$
L	half distance between the supports at the ends of the wire
L_{IN}	half length of the wire when unstrained
L_T	half length of the wire under generic tension T
ΔL	$= L_T - L$
m	disk mass
P	disk weight
r	ω/ω_0

T	tension in the wire $= EA(L_T - L_{IN})/L_{IN} = T_0 + EA(\Delta L/L_{IN})$ $\cong T_0 + EA(\Delta L/L)$
T_0	reference tension in the wire, corresponding to its horizontal disposition $= EA\varepsilon_0$
$\mathbf{T}$	period of the solutions of the equations of motion
$\mathbf{T}_s$	$= 2\pi/\omega$: period of driving rotation
$\bar{u}, \bar{v}$	dimensionless coordinates of C: $u = x/L$; $v = y/L$
$\bar{u}', \bar{v}'$	$\mathrm{d}\bar{u}/\mathrm{d}\tau, \mathrm{d}\bar{v}/\mathrm{d}\tau$
$\bar{u}'', \bar{v}''$	$\mathrm{d}^2\bar{u}/\mathrm{d}\tau^2, \mathrm{d}^2\bar{v}/\mathrm{d}\tau^2$
u, v	$(\sqrt{\mu}/r)\bar{u}, (\sqrt{\mu}/r)\bar{v}$
u', v'	$\mathrm{d}u/\mathrm{d}\tau, \mathrm{d}v/\mathrm{d}\tau$
u'', v''	$\mathrm{d}^2u/\mathrm{d}\tau^2, \mathrm{d}v/\mathrm{d}\tau$
x, y	coordinates of the disk centre in a fixed reference
ε_0	$= (L - L_{IN})/L_{IN}$
μ	coefficient of non-linear terms $= EA/2T_0$
σ	viscous damping coefficient
σ_{cr}	critical value of the viscous damping coefficient $= 2\sqrt{2T_0m/L}$
σ_e	external viscous damping coefficient
σ_i	internal viscous damping coefficient due to hysteresis
τ	ωt
ζ	$\sigma/\sigma_{\mathrm{cr}}$ ratio
ζ_e	$\sigma_e/\sigma_{\mathrm{cr}}$ ratio
ζ_i	$\sigma_i/\sigma_{\mathrm{cr}}$ ratio
ω	angular speed of the rotor
ω_0	natural frequency of the linearized system (about the reference disposition assumed with the wire horizontally taut between the supports).

References

1. Dimentberg, F. M., *Flexural Vibrations of Rotating Shafts*, Butterworths, London, 1961.
2. Ehrich, F. E., 'Shaft whirl induced by rotor internal damping', *Transactions of the ASME, Journal of Applied Mechanics*, 1964, 279–282.
3. Yamamoto, T., Ishida, Y., and Kawasumi, J., 'Oscillations of a rotating shaft with symmetrical nonlinear spring characteristics', *Bulletin of JSME* **18**(123), 1975, 965–975.
4. Ueda, Y., 'Randomly transitional phenomena in the system governed by Duffing's equation', *Journal of Statistical Physics* **20**(2), 1979, 181–196.
5. Ueda, Y., 'Steady motions exhibited by Duffing's equation: A picture book of regular and chaotic motions', in *Approaches to Nonlinear Problems in Dynamics*, SIAM, Philadelphia, PA, 1980, pp. 311–322.
6. Ueda, Y., 'Explosions of strange attractors exhibited by Duffing equation', *Annals New York Academy of Sciences* **357**, 1980, 422–434.
7. Ueda, Y. and Akamatsu, N., 'Chaotically transitional phenomena in the forced negative-resistance oscillator', *IEEE Transactions on Circuits and Systems* **28**(3), 1981, 217–224.
8. Childs, D. W., 'Fractional-frequency rotor motion due to nonsymmetric clearance effects', *Transactions of the ASME, Journal of Engineering for Power* **104**, 1982, 533–541.
9. Sato, S., Sano, M., and Sawada, Y., 'Universal scaling property in bifurcation structure of Duffing's and of generalized Duffing's equations', *Physical Review A* **28**(3), 1983, 1654–1658.
10. Parlitz, U. and Lauterborn, W., 'Superstructure in the bifurcation set of the Duffing equation $\ddot{x} + \mathrm{d}\dot{x} + x + x^3 = f\cos(\omega t)$', *Physics Letters* **107A**(8), 1985, 351–355.
11. Saito, S., 'Calculation of nonlinear unbalance response of horizontal Jeffcott rotors supported by ball bearings with radial clearance', ASME Paper, No. 85-DET-33, 1985.
12. Wolf, A., Swift, B. J., Swinney, L. H., and Vastano, A, 'Determining Lyapunov exponents from a time series', *Physica* **16D**, 1985, 285–317.
13. Press, W., Flannery, B. P., Teukolsky, S. A., and Vetterling, W. T., *Numerical Recipes*, Cambridge University Press, Cambridge, 1986.
14. Szemplinska-Stupnicka, W. and Bajkowski, J., 'The 1/2 subharmonic resonance and its transition to chaotic motion in a non-linear oscillator', *International Journal of Non-Linear Mechanics* **21**(5), 1986, 401–419.
15. Choi, Y. S. and Noah S. T., 'Nonlinear steady-state response of a rotor-support system', *Transactions of the ASME, Journal of Vibration, Acoustics, Stress, and Reliability in Design* **109**, 1987, 255–261.
16. Szemplinska-Stupnicka, W., 'Secondary resonances and approximate models of routes to chaotic motion in non-linear oscillators', *Journal of Sound and Vibration* **113**(1), 1987, 155–172.

17. Pezeshki, C. and Dowell, E. H., 'On chaos and fractal behavior in a generalized Duffing's system', *Physica D* **32**, 1988, 194–209.
18. Ishida, Y., Ikeda, T., Yamamoto, T., and Murakami, S., 'Nonstationary vibration of a rotating shaft with nonlinear spring characteristics during acceleration through a critical speed (A critical speed of a 1/2-order subharmonic oscillation)', *JSME International Journal*, Series III, **32**(4), 1989, 575–584.
19. Shaw, J. and Shaw, S. W., 'Instabilities and bifurcations in a rotating shaft', *Journal of Sound and Vibration* **132**(2), 1989, 227–244.
20. Chiang, I. F. and Noah S. T., 'A convolution approach for the transient analysis of locally nonlinear rotor systems', ASME Paper 90-WA/APM-21, 1990.
21. Kim, Y. B. and Noah, S. T., 'Bifurcation analysis for a modified Jeffcott rotor with bearing clearances', *Nonlinear Dynamics* **1**, 1990, 221–241.
22. Szemplinska-Stupnicka, W., *The Behaviour of Nonlinear Vibrating Systems*, Kluwer Academic Publishers, Dordrecht, the Netherlands, 1990.
23. Ehrich, F. E., 'Some observations of chaotic vibration phenomena in high speed rotordynamics', *Transactions of the ASME, Journal of Vibration and Acoustics* **113**, 1991, 50–57.
24. Olson, C. L. and Olsson, M. G., 'Dynamical symmetry breaking and chaos in Duffing's equation', *American Journal of Physics* **59**(10), 1991, 907–911.
25. Shaw, J. and Shaw, S. W., 'Non-linear resonance of an unbalanced shaft with internal damping', *Journal of Sound and Vibration* **147**(3), 1991, 435–451.
26. Choi, Y. S. and Noah, S. T., 'Mode-locking and chaos in a modified Jeffcott rotor with a bearing clearance', in *Winter Annual Meeting of the American Society of Mechanical Engineers*, Anaheim, CA, ASME Design Engineering Division DE v 50, 1992, pp. 21–28.
27. Ishida, Y., Yamamoto, T., and Murakami, S., 'Nonstationary vibration of a rotating shaft with nonlinear spring characteristics during acceleration through a critical speed (A critical speed of a 1/3-order subharmonic oscillation)', *JSME International Journal*, Series III, **35**(3), 1992, 360–368.
28. Abu-Mahfouz, I. A., 'Routes to chaos in rotor dynamics', Ph.D. Thesis, Case Western Reserve University, 1993.
29. Chang, C. O. and Cheng, J. W., 'Non-linear dynamics and instability of a rotating shaft disk system', *Journal of Sound and Vibration* **160**(3), 1993, 433–454.
30. Genta, G., Delprete, C., Tonoli, A., and Vadori, R., 'Conditions for noncircular whirling of nonlinear isotropic rotors', *Nonlinear Dynamics* **4**, 1993, 153–181.
31. Ishida, Y., 'Nonlinear vibrations and chaos in rotordynamics', *JSME International Journal*, Series C, **37**(2), 1994, 237–245.
32. Adiletta, G., Guido, A. R, and Rossi, C., 'Chaotic motions of a rigid rotor in short journal bearings', *Nonlinear Dynamics* **10**, 1996, 251–269.